Fuel 401 (2025) 135866

Contents lists available at ScienceDirect

Fuel

journal homepage: www.elsevier.com/locate/fuel

Full Length Article

Thermogravimetric and microstructural analysis of the low-temperature oxidation of iron powders☆

Quentin Fradet [a,*], Syafinah Fong [a], Michalina Kurnatowska [a], Antonio Soria-Verdugo [b], Laurine Choisez [c], Uwe Riedel [a]

[a] German Aerospace Center (DLR), Institute of Low-Carbon Industrial Processes, Walther-Pauer-Straße 5, Cottbus 03046, Germany
[b] Department of Thermal Engineering and Fluid Mechanics, University Carlos III of Madrid, Butarque 15, 28911 Madrid, Spain
[c] UCLouvain, Institute of Mechanics, Materials and Civil Engineering, IMAP, Place Sainte 2, B-1348 Louvain-la-Neuve, Belgium

ARTICLE INFO

Keywords:
Iron powder
Metal fuel
Thermogravimetric analysis
Oxidation kinetics

ABSTRACT

Metal fuels, particularly iron, hold great promise as a sustainable source for decarbonating heat or electricity supply. However, a comprehensive understanding of the physics governing the combustion of iron dust flames is currently lacking. In this study, we present a thorough kinetic investigation of the oxidation of iron micrometer particles. Thermogravimetric analysis experiments were conducted under isothermal conditions and with varying uniform heating rates, with air, and with pure oxygen, as well as with various Fe powders. Our results indicate that the oxidation of iron particles can achieve completion at relatively low temperatures, even before the appearance of wüstite. Microstructural analysis suggests an oxidation process under 570 °C dominated by the growth of a duplex magnetite layer, surrounded by a network of hematite ridges. In later stages of oxidation, an inter-particle continuous surface might form, hindering the contact between the iron material and the oxidizing agent. A kinetic analysis has been conducted using model-free and model-fitting methods. An approximate activation energy of 220 kJ/mol has been derived from the Kissinger-Akahira-Sunose method and it is shown that the truncated Sestak and Berggren model could fairly reproduce isothermal and dynamic thermogravimetric analysis experiments.

1. Introduction

Metals and their oxides can be used in oxidation–reduction cycles for large-scale power generation, resulting in CO_2-free energy conversion [1,2]. Recent research efforts have been in particular put on iron [3], as its dry oxidation comes with limited nanoparticle formation in contrast to other metal fuels. Further advantages of iron include its large abundance, relatively low costs and safety hazards. Iron-based combustion technology is quickly developing and currently reaching the MW level [4], but the room for improvement is important, including minimizing material losses, maximizing fuel conversion, avoiding slag accumulation, or optimizing the cyclability of the process.

Combustion modeling, for example with computational fluid dynamics (CFD) simulations, has become an essential tool for optimizing burner design and performance. However, this requires an accurate model for the oxidation kinetics, which is currently lacking. After a certain run-away temperature [5], the process is mostly limited by oxygen diffusion, but a crucial part of the process is governed by a slower kinetic phenomenon. Mich et al. [6] tested three different oxidation models and showed that they led to very different reaction front speeds, which greatly influenced the overall combustion behavior. Ning et al. [7] further showed that small particles are less likely to ignite compared to larger ones. Before ignition of the particles, a passive oxide layer thickens and suppresses oxidation. Therefore, it is crucial to accurately model the particle of oxidation from the early stage of oxide growth. But studies tackling the oxidation kinetics of iron particles are scarce. Therefore, recent works on the combustion of iron dust rely on well-established kinetic data derived from oxidation experiments on iron strips. But to which extent those are transposable for micron-sized particles is an open question. The main objective of the present study is to provide a first understanding of the oxidation of iron and derive first kinetic data. It should shed light on the species in presence, on the rate limiting steps, and on the oxide growth mechanism. A particular focus is put on the “low” temperature oxidation, meaning up to 570 °C. Two

---

☆ This article is part of a special issue entitled: ‘Renewable Metal Fuels’ published in Fuel.

* Corresponding author.

E-mail addresses: quentin.fradet@dlr.de (Q. Fradet), asoria@ing.uc3m.es (A. Soria-Verdugo), laurine.choisez@uclouvain.be (L. Choisez).

https://doi.org/10.1016/j.fuel.2025.135866
Received 28 February 2025; Received in revised form 21 May 2025; Accepted 31 May 2025

main reasons drove this choice. First, even though the mechanism of oxidation below and above this threshold should bear many similarities, this temperature is a threshold for the appearance of wüstite, and thus this choice facilitates the understanding and model development, which can in the future be extended to higher temperatures. Secondly, high temperatures promote sintering, which impact the oxidation process. Recent studies [8,9] show that this effect really starts to prevail above around 600 °C. Thus, the current choice is made to ensure the derivation of the intrinsic growth kinetics.

This paper opens with a dedicated section on the literature on iron oxidation, because metal oxidation in general is an already thoroughly studied research topic, and while peculiarities are associated to the oxidation of powders, the governing physics should essentially be common. Therefore, this section first reviews the theory of metal oxidation, then the current state of understanding of the oxidation of iron strips is presented, and finally the few studies on iron particle oxidation are examined. The next section briefly presents the material, experimental methods, and modelling approaches utilized in this study. Briefly summarized, the kinetic study is based on a comprehensive thermogravimetric analysis (TGA) test campaign consisting of approximately 60 individual experiments on two iron samples of about 8 μ m diameter, particle characterization with scanning electron microscopy (SEM) and X-ray diffraction (XRD) analysis, and standard gas–solid kinetic methods. In the last section, the results are presented and further interpreted to propose a mechanism for the oxidation process of micron-sized particles.

2. Literature review on the oxidation of iron

Oxidation of metals occurs when exposed metallic surfaces come into contact with oxidizing elements, typically oxygen [10]. This process is initiated by the adsorption and chemisorption of oxygen onto the metallic surface. As the coverage progresses, a primary oxide layer forms through nucleation and lateral growth, covering the entire surface [11]. Once established, further growth of the oxide layer can occur if the transport of ions and electrons across the oxide film is possible.

For this transport to happen, points defects within the oxide film are necessary. Those defects are typically vacant lattice sites (for example, a cation vacancy in the cation sub-lattice paired with an anion vacancy in the anion sub-lattice). Ions can jump to surrounding point defect sites, which eventually induces a migration from the metal/oxide interface to the oxide/air interface. Electrons must also migrate to the oxide/atmosphere interface, where they are involved in oxygen ionization. The electron transport mechanism via vacant sites can be slow because of electrical neutrality, but electron migration can be much faster when ions, generally cations, exhibit variable valences. If electron transport is much faster than cation, this creates a negative space charge, which accelerates the migration of cations. The influence of the electric field on the transfer of metal wanes with increasing oxide layer thickness, thus, this mechanism is only valid for thin films. Above a certain transition thickness, whose reference value is 1 μm [12], one speaks of thick film growth. This reference value is only indicative, as it depends from one metal to the other, the conditions of temperature, etc. but it should be noted that it is of a size order comparable to the particle diameters under consideration in this study, i.e., in the order of micrometers. Under the thin film assumption, many theories have been developed leading to multiple rate laws. For example, Mott's initial work [13] suggests that electron tunneling is rate limiting, following a direct logarithmic relationship, while the Cabrera-Mott theory [14] stipulates that at some later stage, ion migration becomes rate limiting, inducing an inverse logarithmic law.

In contrast, for thick films, where space charges play a negligible role, self-diffusion within the oxide film is the primary growth mechanism. This leads to the most known Wagner's theory of thick film growth [15,16]. Among the numerous assumptions, which can be reviewed in Atkinson et al. 1988 [17], it is assumed that diffusion of charged species is rate limiting. The charged species might as well be metal cations, oxygen anions, electrons, or electron holes, depending on the point defects and electronic structure of the oxide. This diffusion supposes a gradient in the chemical potential across the film acting as a driving force. The flux of charged species is inversely proportional to the film thickness, and therefore, a parabolic growth rate is obtained, which has been in many cases experimentally observed [18,19]. However, the oxidation rate is usually several orders of magnitude greater than expected by calculation from the diffusion coefficients. Two main reasons are put forward by Atkinson et al. 1988 [17], the presence of short circuit diffusion pathways through the film and point defect concentrations from the presence of impurities. Short circuits might stem from dislocations, grain boundaries, or interconnected porosity within the oxide [20].

As presently seen, there is a common knowledge base on the oxidation of metals. However, the uniqueness of the individual metals and their oxides makes it necessary to restrain the scope to the iron-oxide system. Iron is arguably the most studied metal when it comes to the oxidation process, spanning from theoretical studies, as iron is the most common metal, to more practical studies on corrosion, as its usage as steel is widespread in all industry applications. The iron-oxide system counts three distinct oxides, with simplified stoichiometric formulas FeO (wüstite), Fe_3O_4 (magnetite), and Fe_2O_3 (hematite). In reality, small deviation from stoichiometry is common, in particular wüstite is metal deficient and presents the peculiarity to be unstable below about 570 °C. Wüstite cation's sub-lattice is composed of ferrous ions Fe^{2+} and hematite of ferric ions Fe^{3+}. Magnetite is composed of both ions in the ratio $Fe^{2+} : Fe^{3+} = 1 : 2$. A general observation made among metals featuring several oxide layers is that the highest oxygen-rich oxide is found in contact with the atmosphere and the lowest in contact with the metal. For iron, this would mean up to three oxide layers $FeO - Fe_3O_4 - Fe_2O_3$ (in order starting from the metal) with oxygen accounting for 22.3, 27.6, and 30.1 $\%_{wt}$ in their stoichiometric forms, respectively. This has been indeed reported for temperatures above 570 °C [18]. The scales (usual name given to the oxide film of important size) are primarily made of wüstite, then magnetite, and a very thin layer of hematite, sometimes even ignored. The exact ratio between the oxides depends on the temperature, oxygen partial pressure, and characteristics of the iron specimen, but nearly constant values of 95:4:1 % are reported above 700 °C [18,19,21,22].

At lower temperatures (that means between 225 and 570 °C, the particular focus of this study), only magnetite and hematite form. Around 225 °C, a majority of hematite is observed, but the proportion of hematite decreases with increasing temperature [23]. At 500 °C, up to ten times more magnetite than hematite has been reported [24]. At 550 °C, the thickness ratio of hematite to magnetite approaches a value of 5 % [25]. But the scale structures forming under this temperature range and the associated kinetic rates are significantly influenced by the preparation of the samples [26,27]. Generally, cold-worked samples exhibit much faster oxidation, especially in the initial stages, compared to annealed samples. This can be attributed to the gradual reduction in contact between the scale and the iron substrate. In areas where the scale remains in contact, it appears relatively thick, whereas in locations where the scale-iron contact is lost, it appears very thin. In extreme cases, certain regions, where the scale-iron contact was entirely lost, showed a unique hematite layer. Many authors also found a duplex magnetite layer [25,28–30]. A duplex layer designates two structurally distinct layers of a same oxide. Atkinson et al. [12] thoroughly described their structure and possible formation mechanism. The outer layer has a columnar structure formed by the outward diffusion of metal ions while the inner layer is more equiaxed and grows by the inward short-circuit transport of oxygen.

As magnetite might be the prevalent oxide in the condition of the present study, a particular attention can be put on the rate-controlling transport mechanisms within magnetite films. In the early study of

Davies et al. [18], the authors estimated that 80 % of the oxide growth was due to oxygen anion diffusion and 20 % from ferrous ion diffusion. But a footnote in a paper from Himmel et al. [31] indicates that there might have been an interpretation error. Bruce [10] compared the self-diffusion coefficient of iron in magnetite and that of oxygen in magnetite and found that the latter is 10^4 lower at 500 °C, concluding that the oxygen diffusion plays a minor role in the growth of magnetite. Limitations to this analysis are that it does not account for short circuit pathways, and the diffusion coefficient for iron was extrapolated from the temperature range 800–1000 °C to 500 °C. But, this suggestion is further supported by the research of Bertrand et al. [29], who performed oxidation tests on pure iron sheets at low temperatures (260–400 °C). They determined that the rate-controlling step in oxidation kinetics is cation diffusion in the outer magnetite layer of the duplex structure. The thickness of this layer controls the amount of inward diffusion of oxygen through its short circuits, ultimately controlling the growth kinetics of the internal magnetite layer. According to their mechanism, the growth rates of the various oxide layers depend on each other and this explains why the proportion of the ratio of oxide layers thicknesses remains constant. At an early stage, before the nucleation of a hematite layer, magnetite might form directly at the magnetite/air interface [32]. This growth subsequently slows down when the hematite layer has nucleated. Thereafter, the oxygen partial pressure for the magnetite outward growth corresponds to the dissociation pressure of hematite. Magnetite forms by the reduction of the overlying hematite layer:

$$Fe^{n+} + n\ e^- + 4\ Fe_2O_3 \rightarrow 3\ Fe_3O_4. \tag{1}$$

As previously mentioned, the oxide growth rates are greater than those calculated from Wagner's theory. Deviations are particularly important below 570 °C. Furthermore, the values are scattered. However, the proposed activation energies, that means the dependency of these growth values with the temperature, are in a rather narrow range: 105 kJ/mol [33] for a temperature range of oxidation of 250–350 °C, 149 kJ/mol [34] for the range 250–375 °C, 134 kJ/mol [35] for the range 200–400 °C, 151 kJ/mol [29] for the range 260–500 °C, 130 kJ/mol [36] for the range 450–550 °C. These values are considerably smaller than the self-diffusion coefficient of iron in magnetite (230 kJ/mol) [31]. All above elements suggest the strong contribution of short circuits in the growth mechanism.

The formation of hematite is often overlooked, especially because of the negligible quantity formed at high temperatures. However, its absence or presence greatly influences the overall growth rate, and thus understanding its formation mechanism is also of importance. One condition for its presence might be that the magnetite grows to a certain thickness so that this layer growth rate falls behind the nucleation of hematite [23]. The nucleation of hematite seems to increase with the oxygen partial pressure [32]. As the growth of hematite is promoted, the growth of magnetite decreases, and thus the overall growth deteriorates. The growth of hematite can as well be achieved by the migration of iron cation to the hematite/air interface, as by the inward migration of oxygen anions to the magnetite/hematite interface. The report growth values are here also several times larger than both the self-diffusion coefficients of oxygen and iron in hematite [31,37]. This external layer of hematite is described as being made of equiaxed grains [29], only a few grains thick [25]. Externally, a network of ridges forms a cellular or honeycomb pattern [21,24]. Many studies also report the presence of whiskers/blades/nanowires growing out of the surface oxide. Those consist of single hematite crystals [38] and could be found under various conditions of oxidizing environment with temperatures comprised between 400 to 800 °C [39]. The presence of water vapour strongly influences the morphology of hematite and promotes the blade formation [30]. These blades might grow from the surface diffusion of iron cations from the underlying magnetite through the tunnels to the blade tips [40,41]. Interestingly, such nanowires have been reported on iron microparticles oxidized in ambient air at 255 °C [42], here also purely composed of hematite.

To conclude this literature review, the focus will now be put on the so-far published works on the oxidation of iron particles. The publication of Lysenko et al. [43] investigated the kinetics of iron powder oxidation using thermogravimetric analysis, however on particles in the nanometer range. Three samples with mean particle sizes ranging from 90 to 350 nm were studied. The samples were always oxidized below 570 °C. The composition analysis of the products revealed the presence of magnetite and hematite. The authors concluded that a three-step process was taking place, with competing oxidation from Fe to hematite or magnetite, and the ultimate oxidation from magnetite to hematite. This was their explanation for the apparent two-stage oxidation under linear increase of the temperature. But a publication also using nanoparticles supplied by a Russian commercial company and made by the electric explosion of wire, revealed a bimodal distribution of the powders [44], which might explain the TGA profiles. Indeed, it is quite apparent that the particle size is a primary influence parameter of the oxidation rate. Mandilas et al. [45] performed TGA on nanoparticles, with mean sizes between 25 and 85 nm and one TGA experiment with a reference sample between 6 and 10 μm. The TGA curve under linear temperature increase of the sample with micrometer particles is shifted by about 150 °C compared to the samples with nanometer particles and a plateau is reached at about 570 °C. Similar conclusions can be drawn from the publications of Zhang et al. [46] and Korshunov [47], where nano and micrometer iron powders are compared. Mandilas et al. [45] further studied the effect of oxygen concentration and found that increasing the oxygen content from 2 % to 21 % accelerated oxidation, but no notable differences were identified between synthetic air and pure oxygen environments. In another paper, Lysenko et al. [48] showed that the presence of 20 % wüstite in the original powder shifts the TGA curves using a constant heating rate to higher temperatures (at least 200 °C), meaning that the reactivity of the iron powder was drastically reduced by the presence of wüstite. More recently, Kuhn et al. [9] investigated the oxidation behavior of iron particles in the micrometer range based on thermogravimetric analysis. They showed the dependency of the rate of oxidation with both the particle size and the oxidation temperature. The authors further demonstrated that the cyclization of iron particles enhances reactivity, which they attributed to increased porosity of the particles. Spielmann et al. [8] conducted isothermal oxidation of micrometer-sized iron particles in the temperature range 600–700 °C and followed by post-mortem Mössbauer spectroscopy. They notably observed a two-step process, with a rapid initial oxidation, followed by a slower second phase, which can be described by the parabolic rate law.

3. Materials and methods

3.1. Thermogravimetric experiments

Two iron powder samples have served for the purpose of this article. The first sample used in this experiment was a commercial iron powder obtained from Carl Roth GmbH, Karlsruhe, Germany (article N° 3718.1). It has a mean diameter of 8 μm and a purity level exceeding 99.5 % [49]. The second sample was also carbonyl iron powder, but from Sigma-Aldrich (product number 12310), with a purity level above 99 %. Though it can be found in the literature that this powder is composed of much larger particles with a mean diameter of 120 μm [50], our analysis revealed a particle size distribution very close to the powder from Carl Roth. Details on the conducted analysis and the results will be given in Sections 3.2 and 4.1. In the following, powders A and B designate the samples from Carl Roth and Sigma-Aldrich, respectively.

A comprehensive TGA test campaign on the oxidation behavior of the previously mentioned powders was conducted. The detailed list of experiments is given in Table 1. This list also gives the corresponding figures to each experimental set, that they are to be found in the remainder of the paper or in the Supplementary Materials. Two different

Table 1
Thermogravimetric experiments conducted in this study and the corresponding operating conditions.

Denomination of experiment groups	TGA device	Sample and mass	Gas conditions	Temperature conditions	Associated figure(s)
Q500_PA_Air_Iso	TA Instruments Q500	Powder A ∼28 mg	Air 60 mL/min	Isothermal 300, 350, 400, 450, 500, 550 °C	Fig. 2 Fig. S3 Fig. S5
PT1600_PA_Air_Iso	Linseis TGA PT 1600	Powder A ∼28 mg	Air 100 mL/min	Isothermal 300, 350, 400, 450, 500, 550 °C	Fig. S4
Q500_PB_Air_Iso	TA Instruments Q500	Powder B ∼28 mg	Air 60 mL/min	Isothermal 300, 350, 400, 450, 500, 550 °C	Fig. 2 Fig. S3 Fig. 13 Fig. S4 Fig. S5
PT1600_PB_Air_Iso	Linseis TGA PT 1600	Powder B ∼28 mg	Air 100 mL/min	Isothermal 300, 350, 400, 450, 500, 550 °C	Fig. S4
PT1600_PB_Air_Flow	Linseis TGA PT 1600	Powder B ∼28 mg	Air 20, 200 mL/min	Isothermal 400 °C	Fig. 3
Q500_PA_Air_Iso_HighT	TA Instruments Q500	Powder A ∼28 mg	Air 60 mL/min	Isothermal 570, 600, 650, 700 °C	Fig. S4
PT1600_PAB_Air_Step	Linseis TGA PT 1600	Powder A & B ∼28 mg	Air 100 mL/min	Stepwise Isothermal 300–400-500 °C	Fig. 4
Q500_PB_O2_Iso	TA Instruments Q500	Powder B ∼28 mg	O_2 60 mL/min	Isothermal 300, 350, 400,450, 500, 550 °C	Fig. 5 Fig. S7
Q500_PB_Air_Lin	TA Instruments Q500	Powder B ∼28 mg	Air 60 mL/min	Linear increase 1, 2, 5, 10, 15 °C/min	Fig. 6 Fig. 11 Fig. 12
PT1600_PA_Air_Lin	Linseis TGA PT 1600	Powder A ∼28 mg	Air 100 mL/min	Linear increase 1, 2, 5, 10, 15 °C/min	Fig. S8
PT1600_PB_Air_Lin	Linseis TGA PT 1600	Powder B ∼28 mg	Air 100 mL/min	Linear increase 1, 2, 5, 10, 15 °C/min	Fig. S8
Q500_PB_O2_Lin	TA Instruments Q500	Powder B ∼28 mg	O_2 60 mL/min	Isothermal: 300, 350, 400, 450, 500, 550 °C	Fig. 6 Fig. 11 Fig. 12
PT1600_PA_Air_Iso_HighM	Linseis TGA PT 1600	Powder A ∼300 mg	Air 100 mL/min	Isothermal 400 °C	Fig. S6 Fig. 7 Fig. 8 Fig. 10
PT1600_PAB_Air_Lin_HighM	Linseis TGA PT 1600	Powder A & B ∼300 mg	Air 100 mL/min	Linear increase 5 °C/min	Fig. S6 Fig. 7 Fig. 10

TGA instruments – a Linseis STA PT 1600 apparatus and a thermogravimetric analyzer TGA Q500 from TA Instruments – were used and most of the tests have been conducted multiple times to ensure their reproducibility. Aluminium oxide crucibles (purity: 99.7 %, height: 3.7 mm, diameter: 6.8 mm, volume: 0.12 ml) were used when conducting the tests with the Linseis STA PT 1600 apparatus. A photograph of the test setup using an alumina crucible is shown in Fig. S1 of the Supplementary Materials. Flat platinum sample pans (diameter: 10 mm, volume: 0.1 ml) were used for both non-isothermal and isothermal tests with the TGA Q500 analyzer, and the sample initially of about 28 mg was homogenously distributed on the pan to improve the contact of the sample with oxygen. Non-isothermal and isothermal experimental measurements were performed. For non-isothermal oxidation tests, a linear increase in temperature from ambient to 900 °C was used, at constant heating rates of 1, 2, 5, 10, and 15 °C/min. Isothermal oxidation was also studied, increasing the temperature from ambient to the oxidation temperature, while supplying the furnace with a flow rate of nitrogen to guarantee inert conditions for the sample until the desired temperature was reached. Then with the TGA Q500 analyzer, the flow was suddenly changed to supply the oxidizing gas, either air or pure oxygen, at a constant temperature for at least 60 min, while with the Linseis STA PT 1600 apparatus, a dwell time of 20 min with nitrogen gas was respected and then gradually changed to oxidizing gas within 6 s. The oxidation temperatures tested for the isothermal experiments range from 300 to 700 °C, with a particular focus on the range 400–570 °C. The tests were performed by supplying a constant flow rate (of 60–100 ml/min in the regular cases) of oxidizing gas, namely air or oxygen, to the furnace. Tests with variations of the gas flow rate and initial solid weight were also conducted to study the effect of the two operating parameters.

3.2. *Microstructural characterization*

To gain further understanding of the oxidation process, the phase distribution and morphology of three different oxidation conditions were characterized:

- after isothermal oxidation at 400 °C for 2 h,
- after linear heating at 5 °C/min up to a temperature of 455 °C, corresponding to roughly 50 % of oxidation according to the mass intake,
- after linear heating at 5 °C/min up to a temperature of 700 °C.

The external morphology of the oxidized samples, which were in contact with the crucible, was observed using a scanning electron microscope Zeiss Ultra55 with a voltage of 5 kV and a secondary electron detector. In addition, the cross-section of a sample oxidized at 400 °C and a sample oxidized up to 700 °C were observed by polishing the pellets to their mid-thickness and using the same SEM with a voltage of 15 kV and a backscattered electron detector. The oxidized samples (each 300 mg) from 4 different tests were then crushed for each experimental condition to amount for at least 1 g of oxidized powder. The phases formed for each experimental condition were identified using an x-ray diffractometer D8 Advance A25-X1, with a cobalt target at 35 kV and 40 mA. The mass distribution of each phase was then quantified by Rietveld refinement using the software Bruker TOPAS Version 5.0.

3.3. Kinetic modeling approaches

The thermal analysis experiments of this paper are reported as the sample mass evolution, more precisely as the ratio of the sample weight at a certain time, $m(t)$, to the initial sample weight, m_0. It is common in gas–solid kinetic methods to rather use the conversion degree, or in the present case, the extent of oxidation α. By assuming the initial sample to be composed of 100 % iron, and taking hematite as the final stage of oxidation, it is defined as:

$$\alpha = \frac{m(t) - m_0}{m_\infty - m_0}, \tag{2}$$

where:

$$m_\infty = \frac{M_{\mathrm{Fe_2O_3}}}{2M_{\mathrm{Fe}}} m_0 \approx 1.4297 m_0. \tag{3}$$

In the previous equation, m_∞ is the theoretical mass after complete oxidation, and M the molar weight. In the present kinetic analysis, it is assumed, as commonly done, that the conversion rate can be expressed according to the general formulation:

$$\frac{\mathrm{d}\alpha}{\mathrm{d}t} = f(\alpha)k(T), \tag{4}$$

where $f(\alpha)$ is the reaction model and $k(T)$ is the rate constant, which represents the dependence of the process rate on temperature, typically expressed by the Arrhenius equation. Among the classical gas–solid kinetic methods, one can make the distinction between two groups of methods, the model-free methods and the model-fitting methods [51,52].

In the first group of methods, no determination of the reaction model is needed, hence their name. One such method is the Kissinger method [53,54], which allows the determination of the activation energy from a series of experiments with varying heating rates β. The method relies on the fact that there is a certain temperature T_{max} where the reaction rate is maximum, and thus the second derivative of the conversion degree with respect to time is zero. The following equation can be derived:

$$\ln\left(\frac{\beta}{T_{max}^2}\right) = \ln\left(-\frac{AR}{E_a}\frac{\mathrm{d}f}{\mathrm{d}\alpha}\right) - \frac{E_a}{RT_{max}}. \tag{5}$$

Plotting the left-hand side of the previous equations against $1/T_{max}$, obtained from experiments with varying heating rates, the activation energy can be derived from the slope. Another model-free method is the Kissinger–Akahira–Sunose (KAS) method [55], which also serves to derive the activation energy from TGA experiments with constant heating rates. The form of the final equation is similar to the one of the Kissinger method:

$$\ln\left(\frac{\beta}{T_\alpha^2}\right) = \mathrm{Const} - \frac{E_a}{RT_\alpha}, \tag{6}$$

but with RT_α, that means the temperature at which a certain conversion degree is reached. Similarly, plotting the left-hand side for a series of experiments versus $1/T_\alpha$ gives the activation energy. Where the Kissinger method yielded a unique activation energy value corresponding to the point of maximum reaction rate, the KAS method can be applied at different values of α, or even continuously from $\alpha = 0$ to α_∞.

The second group of methods, i.e., the model-fitting methods, requires an assumption of the mathematical expression for the reaction model $f(\alpha)$ [56]. Many information can be gathered from a simple reading of the TGA curve profiles under isothermal conditions. Whether they show a decelerating, sigmoidal, or accelerating profile can guide the choice of possible reaction models. Confronting the kinetic data with microstructural analysis can further comfort the model choice [57]. Further testing of different reaction models can be done for isothermal runs by rearranging and integrating Eq. (4):

$$\frac{\mathrm{d}\alpha}{f(\alpha)} = k(T)\mathrm{d}t, \tag{7}$$

$$\int_0^\alpha \frac{\mathrm{d}\alpha}{f(\alpha)} = g(\alpha) = k(T)t. \tag{8}$$

Thus, plotting the integral form, $g(\alpha)$, versus the time for a single experiment should yield a straight line if the right reaction model is picked.

The methods described previously, both model-free and model-fitting, are valid under certain assumptions, notably the process should obey single-step kinetics [56]. Multiple overlapping or consecutive reactions can bring these methods to their limitations. The result section will determine if these methods are suited to this oxidation process.

4. Results and discussion

4.1. Initial powders

Powders A and B are very similar in terms of morphology as illustrated in Fig. 1. They are composed of small near-spherical particles of about ~1–53 µm in diameter, generally forming agglomerates of a few dozen microns. Some larger blocks of 50–100 µm could also be found in both samples. Those have not been considered in the particle size distributions in Fig. 1e. The distributions reveal the large similarity between the two powders, with mean particle sizes of 5 µm. The XRD analysis, also given in the Supplementary Materials, identified α-iron as the only detected phase in both powders.

4.2. Oxidation under isothermal conditions

The major results of the thermogravimetric measurements conducted under isothermal conditions for both powders are presented in Fig. 2. In the interest of clarity and visual representation, the figures presented here and in the following sections depict fewer experimental points than the actual frequency of acquisition. A close-up on the 300 first seconds can also be found in the Supplementary Materials. All curves exhibit a similar shape, with an initial, almost linear, stage of rapid oxidation followed by a second stage with a markedly slower oxidation rate. The slope during the initial stage is nearly identical for all experiments (about 8 percent of weight gain per minute), though a slight increase with temperature can be discerned (Supplementary Material Fig. S3). But the extent of the initial stage increases with the temperature except for the test case 550 °C for powder A, which is an outlier, further detailed in the next paragraph. Specifically, taking powder B as an example, the mass gain at 300 °C after one hour is only 3.3 %, corresponding to an oxidation degree of 7.7 % relative to the maximum theoretical value, while at 550 °C, the mass change is 37.5 %, or, in other terms, the material has oxidized to 87.2 %. The oxidation profiles of powders A and B are similar. Powder A exhibit a slightly faster oxidation rate.

The reproducibility of the experimental results, as well as further data with the second TGA apparatus and for temperatures above 570 °C, are given in Fig. S4. The results are very consistent over several experiment replications for set temperatures from 300 to 500 °C, and for both oxidation stages. The experiments run at 550 °C show more variability. In numerous cases, the first stage stops promptly before the 450 and 500 °C instances, and the second stage is marked with no significant increase in oxidation. These elements suggest that at elevated temperatures, the oxidation is more sensitive to the experimental preparation, such as the even distribution of iron material on the crucible, maybe due to non-uniform oxidation and localized sintering. The results obtained with either apparatus are comparable, and the minor discrepancies can be attributed to the specific flow patterns within the furnace or the shape and material of the crucibles employed. Some results at temperatures

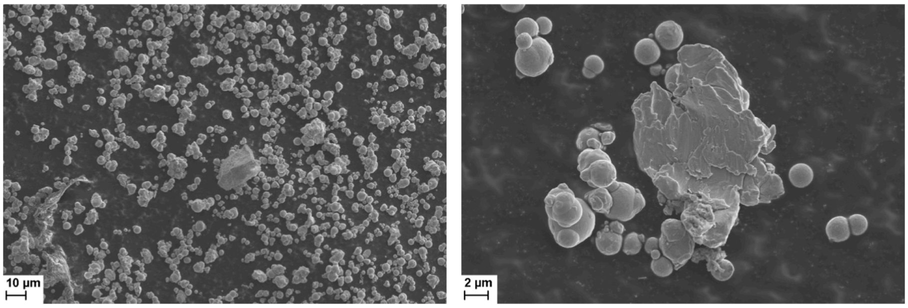

a. Powder A

b. Powder A

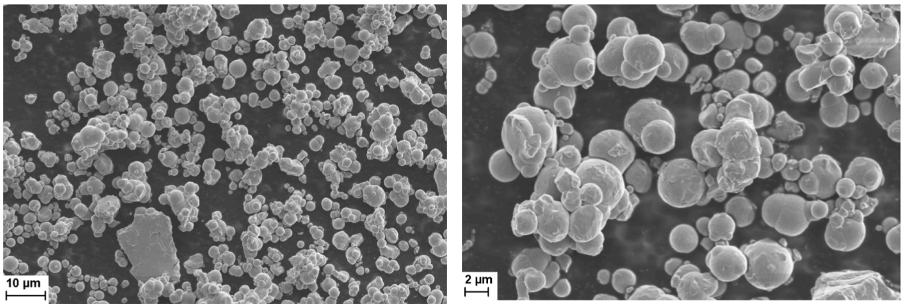

c. Powder B

d. Powder B

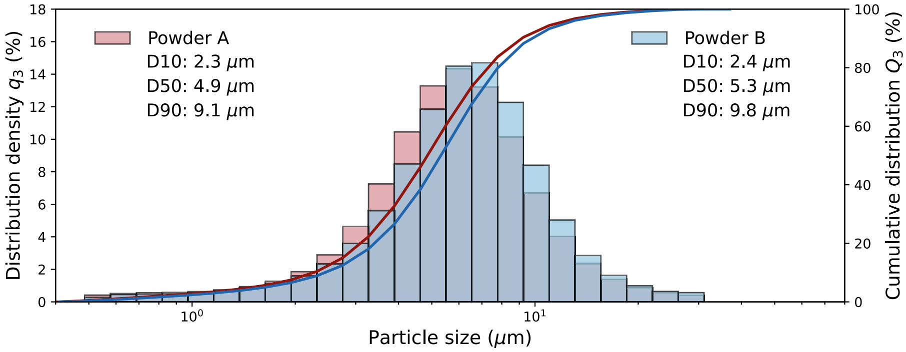

e.

Fig. 1. SEM images of the raw powders as well as particle size distribution by volume of both powders.

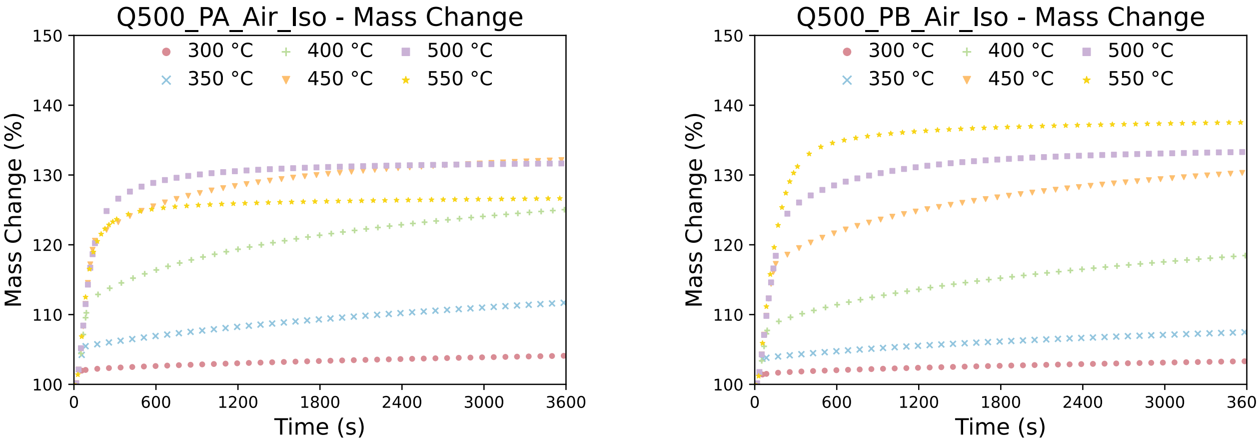

a. Powder A

b. Powder B

Fig. 2. Thermogravimetric analysis of both powders under isothermal conditions.

570 °C and higher are given in Fig. S4. As it does not constitute the focus of the present article, their description is here succinct. Globally, the curve shapes are rather similar to those observed at lower temperatures, with two distinct stages, but in this case, the extent of oxidation does not appear to increase monotonically with increasing temperature. On the opposite, the global trend is a slight decrease from 570 °C to 700 °C.

The variation in temperature over the course of each individual experiment has been recorded. The data are presented in Fig. S5 for the oxidation of both powders. It can be observed that a temperature increase occurs when the gas is switched between the inert and the air atmosphere. This can be attributed to the exothermic nature of the oxidation reactions between iron and air. The temperatures subsequently stabilize to the set temperatures more or less rapidly. The duration of this stabilization period manifestly depends on the duration of the rapid oxidation stage. The amplitude of this temperature offset differs between experiments, and although it represents a mere few degrees, the measurements are acquired via a thermocouple for the gas phase. It can be assumed that the temperature increase for the iron particles is significantly higher.

The effect of air flow rate is shown in Fig. 3. Three different flow rates, with values of 20, 100, and 200 mL/min, have been employed at the same temperature of 400 °C. The slope of each of the three curves is notably different, accounting for, in order, 2.3, 5.5, and 9.1 percentage points of mass gain per minute. The extent of oxidation is greater for the highest flow rate case, but very similar for the two others. The slow oxidation stage proceeds at a similar rate for all experiments. The effect of the sample mass has also been investigated and the results can be seen in Fig. S6. Increasing the sample mass has the inverse effect of increasing the gas flow rate, i.e., the slope of the initial stage decreases. Later on, the sample mass has little importance. The higher extent of conversion for powder A with a high mass can be attributed to result variability.

Fig. 4 depicts the thermogravimetric results obtained by incrementally elevating the temperature (300 °C, then 400 °C, then 500 °C) over the course of one hour at each step with one-hour operation at each temperature. The figure shows that the process, albeit entering a slow oxidation stage, can be re-accelerated by increasing the temperature. Once more, both powders exhibit comparable oxidation behaviors. However, following each temperature increment, two distinctive stages are not identified; rather, a single parabolic decelerating profile is observed. Additionally, it is notable that the extent of oxidation at the end of each temperature interval is slightly higher compared to the regular isothermal experiments (see, for example, Fig. 2).

The effect of utilizing pure oxygen on the oxidation process under isothermal conditions can be appreciated in Fig. 5. Here also, a close-up on the first 300 s and the temperature profiles can be found in the Supplementary Materials. The two stages are more pronounced than with air. Apart from the 300 °C case, which is an outlier, the oxidation initially follows a linear profile, with a slope of approximately 20 $\%_{wt}$ gain per minute, which is approximately 2.5 times faster than with air, while the oxygen concentration is approximately five folds higher. Conversely, the second stage is comparatively slow, approaching near-zero mass increase rates in many cases. With regard to the temperature evolution, it can be observed that the offset is significantly greater than that observed when using air, reaching a value of approximately 20 °C for the 350 °C case (Fig. S7 of the Supplementary Materials).

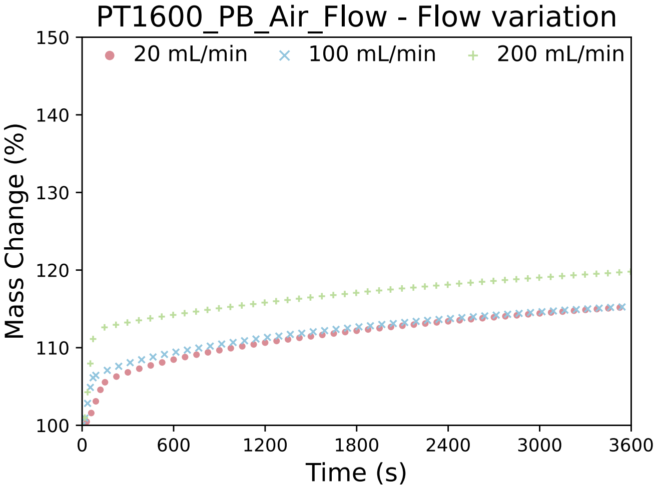

Fig. 3. Variation of the gas flow rate at 400 °C for powder B.

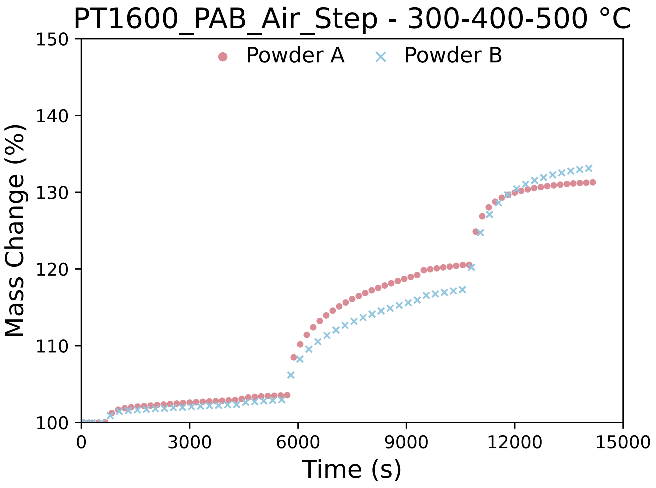

Fig. 4. Thermogravimetric analysis of powders A and B with stepwise temperature increases.

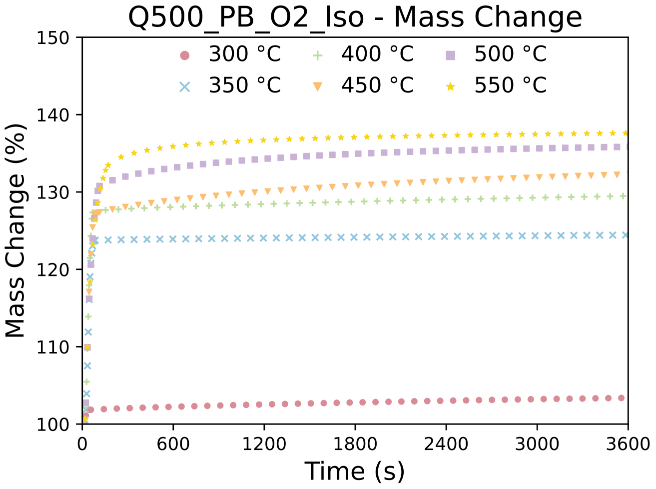

Fig. 5. Thermogravimetric analysis of powder B under isothermal conditions using pure oxygen.

4.3. Oxidation under a constant heating rate

The TGA experiments under linear temperature increase using the Q500 TGA apparatus and powder B are shown in Fig. 6. The mass change for the experiments with air at 1, 2, and 5 °C/min reached 142.7–143.0 %, which corresponds precisely to the theoretical value of the complete oxidation from iron to hematite. The experiments at 10 and 15 °C/min show on the other hand an advanced but incomplete oxidation, 141.1 and 141.3 % at 900 °C, respectively. The oxidation starts in all experiments at around 200 °C. No distinct successive step can be observed, the rate of oxidation gradually increases up to about 500 °C and 50 % of oxidation, then gradually decreases. Fig. 6b shows the derivative of the

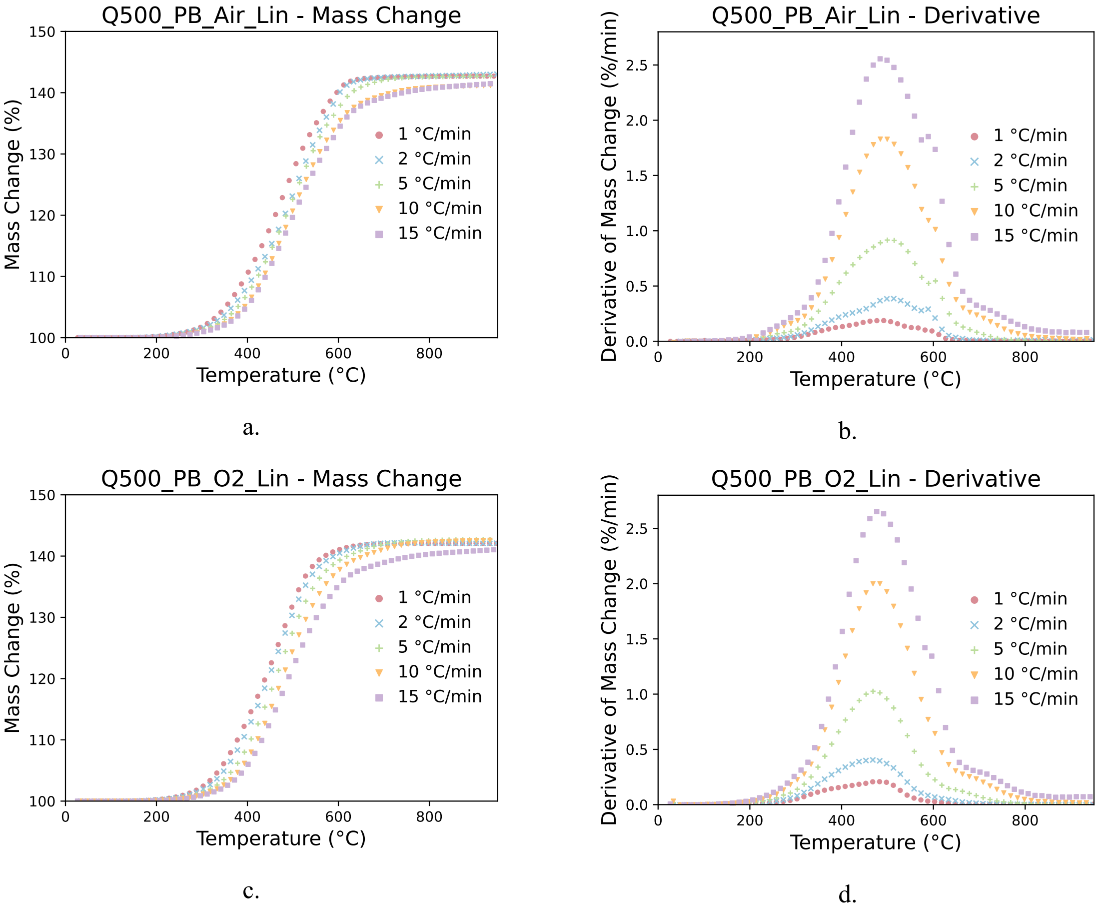

Fig. 6. Thermogravimetric analysis on powder B with constant heating rates from 1 to 15 °C/min in a. air and c. pure oxygen, as well as the derivative of the mass change (b. and d., respectively).

mass change with respect to the temperature for the same experiments as in Fig. 6a. In all experiments, the rate of oxidation increases from 200 to about 500 °C then decreases except for a peak at around 600 °C. This momentary increase in the reaction rate can be related to another reaction pathway involving wüstite above 570 °C.

The results of the TGA experiments with pure oxygen under linear temperature increases and the corresponding derivatives using the TGA Q500 apparatus are also shown in Fig. 6. The curve profiles are very similar to the ones obtained with air. The rate of oxidation is slightly increased by the presence of pure oxygen. The sample of the experiment at 10 °C/min now also undergoes full oxidation. The wüstite peak seems even less important under these conditions and is even not visible for low heating rates. An explanation for this is that the oxidation in the presence of pure oxygen is more advanced or even close to completion at 570 °C.

Further results under constant heating rates can be found in the Supplementary Materials. Fig. S8 shows the TGA curves obtained under constant heating rate with the second analyzer and for both powders. The curves have a similar shape and the extent of oxidation is advanced at the end of the experiments, higher than 135 % in all cases. But it appears more difficult to reach a complete oxidation with the second apparatus, which may find its origin in the difference in crucible shape and material. The influence of the mass variation at a temperature increase of 5 °C/min can be seen in Fig. S6. The curves almost overlap for the larger part of the experiments. A notable difference is that the final extent of oxidation is slightly lower when higher masses are used.

4.4. Microstructural analysis

Fig. 7 shows the external morphology of the oxide crust formed during the oxidation of powder B. A strong variation of the morphology is observed when oxidized under 455 °C or above 700 °C. Under 455 °C (Fig. 7a–b for isothermal 400 °C and Fig. 7c–d for 5 °C/min up to 455 °C), the oxide phase forms around each particle, which can still be distinguished from one another. A porous honeycomb-like scale is observed at the external surface of the particles. The latter is constituted of an external network of smaller hematite grains due to their favored growth along specific crystalline directions, as developed in [57]. A strong inter-particle sintering is also observed, forming a continuous agglomerate. The inner morphology of the oxide layers can be observed in Fig. 7d, where the cross-section of a particle is visible after a local fracture. The grains of the oxide phase present a columnar morphology close to the surface and an equiaxed morphology close to the non-oxidized core. At 700 °C (Fig. 7e–f), a continuous layer of iron oxide is formed across the entire sample, with only few individual particles being distinguished. The same porous honeycomb-like morphology is observed for the external oxide crust, but with a larger size (in the order of magnitude of 500 nm for a single honeycomb structure at 700 °C, and of 100 nm at 400 °C). The size of the hematite grains forming this external network increases therefore with the oxidation temperature. Further SEM images under various magnification for powders A are given the supplementary materials.

The cross-section of a sample oxidized at 400 °C is shown in Fig. 8. Iron can be distinguished in white from the iron oxides in grey from the backscattering contrast used in the SEM. A layer of ~100–130 μm with a lower particle density is formed around the periphery of the sample, as

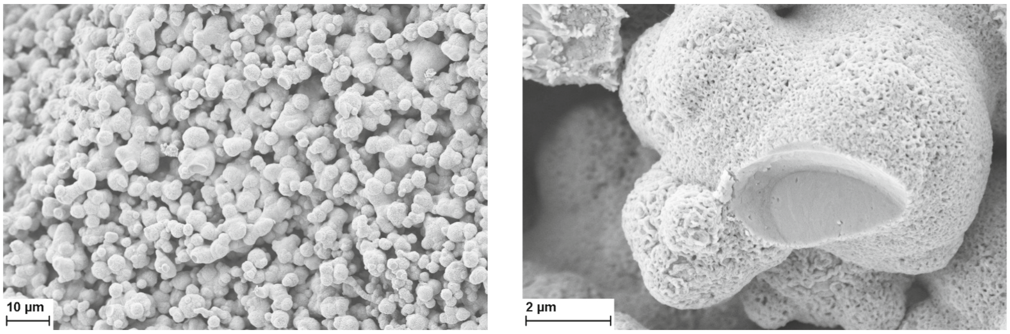

a. Powder B oxidized at 400 °C during two hours

b. Powder B oxidized at 400 °C during two hours

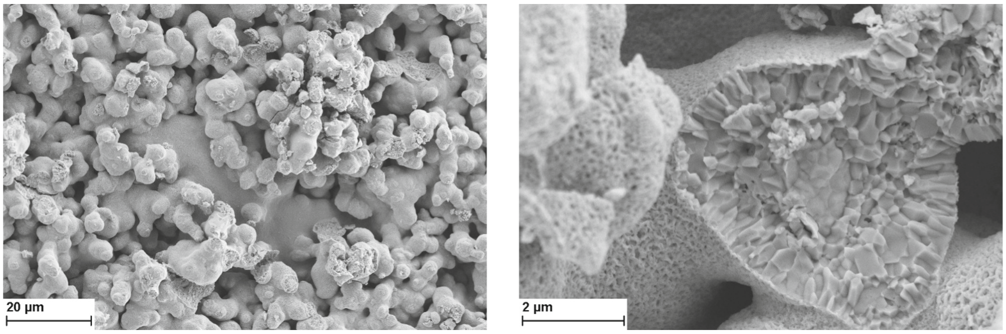

c. Powder B oxidized under a constant temperature increase of 5 °C/min up to an oxidation extent of 50%

d. Powder B oxidized under a constant temperature increase of 5 °C/min up to an oxidation extent of 50%

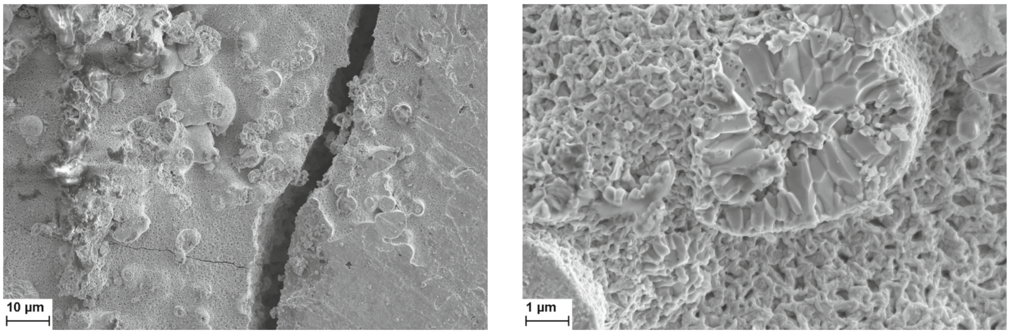

e. Powder B oxidized under a constant temperature increase of 5 °C/min up to a temperature of 700 °C

f. Powder B oxidized under a constant temperature increase of 5 °C/min up to a temperature of 700 °C

Fig. 7. SEM images of the powder B.

visible in Fig. 8a, and magnified in Fig. 8c and e. A porosity of around 38 vol% was estimated in this region using image analysis, while the center of the sample (Fig. 8b, d, and f) is globally less porous (in the order of 9 vol%), with more inhomogeneity between different zones. Interestingly, there is not much difference in terms of oxidation degree between the outer layer and the center. In both cases, the volume phase percentage of iron and iron oxide is around 50 %/50 %. These estimations are based upon image analysis by calculating the surface covered by the light or dark grey regions. Analogous to the SEM image of the broken particle described in the previous paragraph, the SEM images of individual particles (Fig. 8d and e) suggest two distinct magnetite layers. In the case of the cross-sections, individual grains are less visible, but we can see a prominent and dense external oxide layer and a thinner one, partly porous, around the iron cores.

SEM images of the cross-section of a sample oxidized up to 700 °C can also be appreciated in Fig. 9. An external layer (magnified in Fig. 9c and e) can also be distinguished, constituted of a duplex oxide layer, with equiaxed grains close to the inner structure (on about 9 μm) and thinner columnar grains close to the external surface (on about 4 μm). The internal structure (Fig. 9b, d, and f) consists of several iron islands surrounded by equiaxed iron oxide grains and large pores (100–300 nm thick), in a matrix of equiaxed grains presenting a eutectoid microstructure. The latter presents a lamellar structure, with iron lamellae formed in a matrix of iron oxide. This structure reminds the observations of Gleeson et al. [58] of samples oxidized to 900 °C and further cooled down to temperatures between 100 and 500 °C. It originates from the disproportionation reaction of FeO into Fe + Fe_3O_4. In the present experiments, the cooling rate was −28 °C/min during the first 10 min, then, −17 °C/min for next 20 min, and −12 °C/min for 30 min. As the sample approached 200 °C, the cooling rate gradually reduced to −9 °C/min. The cooling process was sufficiently slow to accredit the importance of the disproportionation reaction. The absence of a lamellar structure around the iron grains, could be explained by solid rearrangement with diffusion of Fe towards the existing grain, which could further explain the large pores observed around the grains. A decrease in iron islands is observed moving closer to the external layer, showing an increase in oxidation level near the surface.

The XRD curves and associated phase distribution for the cases isothermal at 400 °C, 5 °C/min up to an oxidation extent of around 50 %, and 5 °C/min up to a temperature of 700 °C with an initial iron weight of

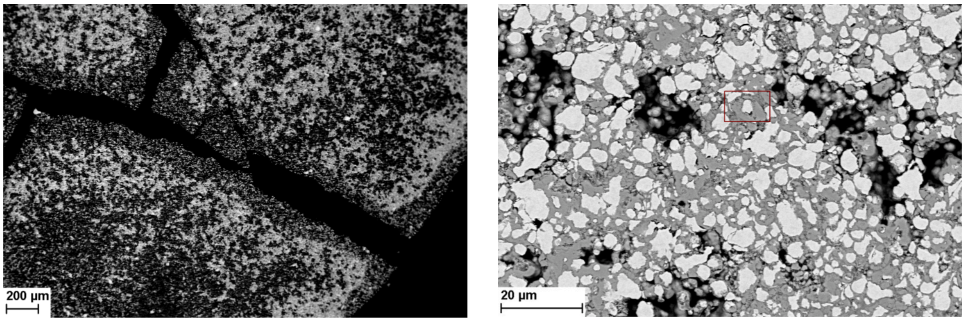

a. Powder Alarge view

b. Powder A center region of the sample

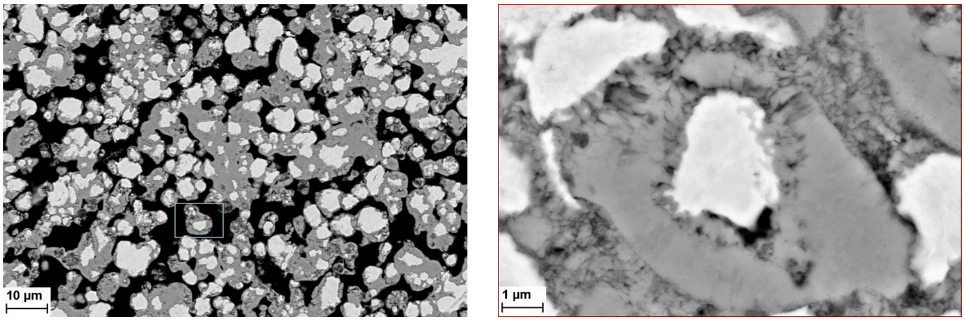

c. Powder A center region of the sample

d. Powder A center region of the sample

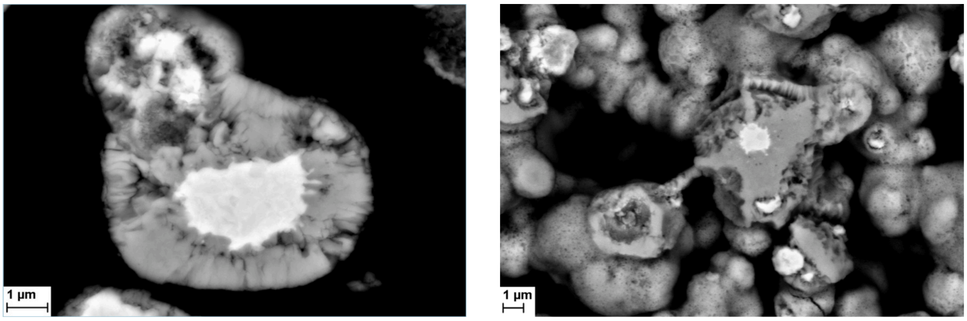

e. Powder A edge of the sample

f. Powder A edge of the sample

Fig. 8. SEM images of the cross-section of powder A oxidized at 400 °C during two hours.

300 mg each are presented in Fig. 10. The oxidation degrees estimated by the XRD analysis are of 57.7, 46.0, and 71.3 %, in the order previously mentioned. In particular, the degree of oxidation of the second sample is very close to the targeted value of 50 %. Under 455 °C, only magnetite and hematite phases are formed, with a ratio (around 5:95 for isothermal oxidation at 400 °C) comparable to the analogous oxidation on iron strips. Wüstite is formed at higher temperatures, with a non-uniform stoichiometry probably corresponding to a gradual oxygen enrichment as wüstite is formed from iron and further oxidizing into magnetite. The sample oxidized at 5 °C/min up to 700 °C shows more than 15 % of iron. This could be due unoxidized iron but can also originate from the decomposition of wüstite into iron and magnetite during the cooling process. XRD results from powder B are given in Fig. S11 of the Supplementary Materials, from which similar conclusions can be drawn.

4.5. *Kinetics of the oxidation process*

Fig. 11 shows the results of the Kissinger–Akahira–Sunose method; a method used to derive the activation energy from TGA experiments with a constant heating rate. The symbol β that appears in the figure corresponds to the heating rate of the individual experiment, i.e. 1 to 15 K/min as labelled in Fig. 6. It was performed with the experiment in air and pure oxygen and at three conversion degrees, 0.25, 0.5, and 0.75. The values found are high, in the range 180–320 kJ/mol. A value of 220 kJ/mol is used in the following.

The decelerating profiles of isothermal tests could be associated with a phase-boundary, a diffusion, or a first-order model. Furthermore, the truncated Sestak and Berggren model is investigated [56]. It assumes a reaction model in the general form:

$$f(\alpha) = \alpha^m (1-\alpha)^n, \tag{9}$$

where m and n are parameters to determine. The effect of the atmosphere was accounted for as follows:

$$\frac{\mathrm{d}\alpha}{\mathrm{d}t} = f(\alpha)k(T)\left(P_{O_2}/P_{tot}\right)^p. \tag{10}$$

These parameters were determined from the experiments with linear temperature increase via the least-square method. The final values read $n = 2.3, m = -3, p = 0.5$. Fig. 12 shows both the modeling results using Eq. (10) and the experiments. The approach gives overall good agreement.

The same model was tested on isothermal experiments and using the parameters previously derived: E_a, n, m, and p. However, the direct calculation of the rate of oxidation as given by Eq. (10) results in an important overestimation in the early stage of oxidation. As it will be further detailed in the next section, the initial stage is limited by the external gas transfer limitation. To take this effect into account, the rate

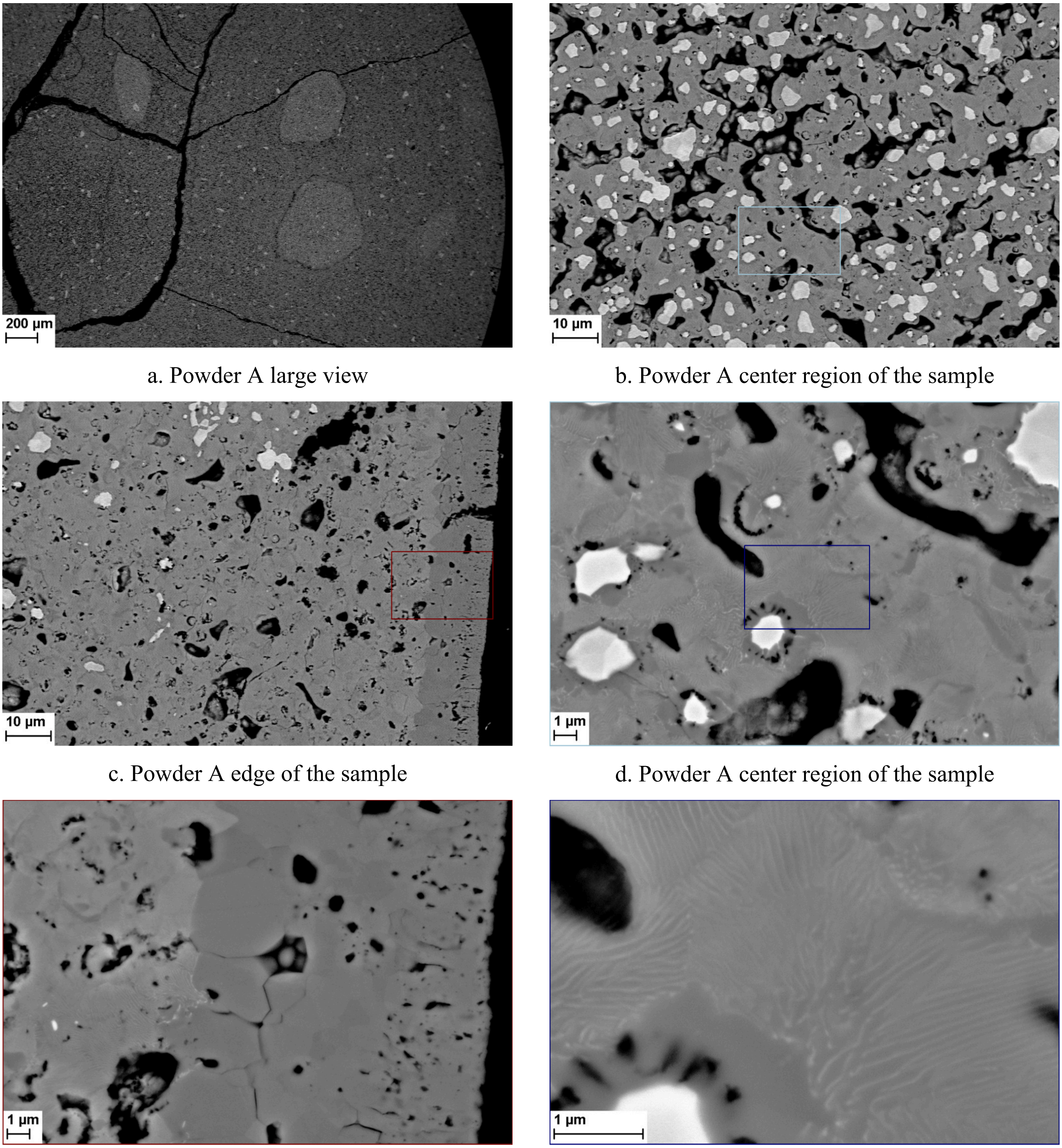

a. Powder A large view

b. Powder A center region of the sample

c. Powder A edge of the sample

d. Powder A center region of the sample

e. Powder A edge of the sample

f. Powder A center region of the sample

Fig. 9. SEM images of the cross-section of powder A oxidized under a constant temperature increase of 5 °C/min up to a temperature of 700 °C.

of oxidation was taken as the minimum between the initial slope (0.0034 s^{-1}) and the value given by Eq. (10), i.e. solid-state process. The results are reported in Fig. 13. It can be seen that good agreements can be obtained in the case of isothermal experiments with the parameters derived previously from dynamic experiments and taking oxygen supply limitations into account. The dependency on the temperature is well retrieved, suggesting a realistic value for the activation energy.

To foster efforts in the development of more detailed kinetic models, the three sets of experiments Q500_PB_Air_Lin, Q500_PB_O2_Lin, and Q500_PB_Air_Iso have been made available as Supplementary Materials. Some directions for improvement include multi-component approaches, or models that consider particle characteristics.

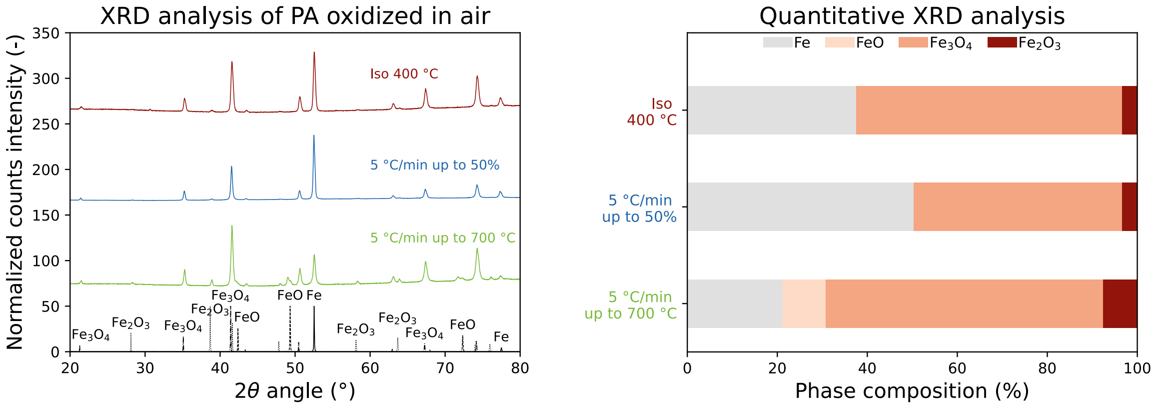

a.

b.

Fig. 10. XRD analysis of powder A oxidized in air.

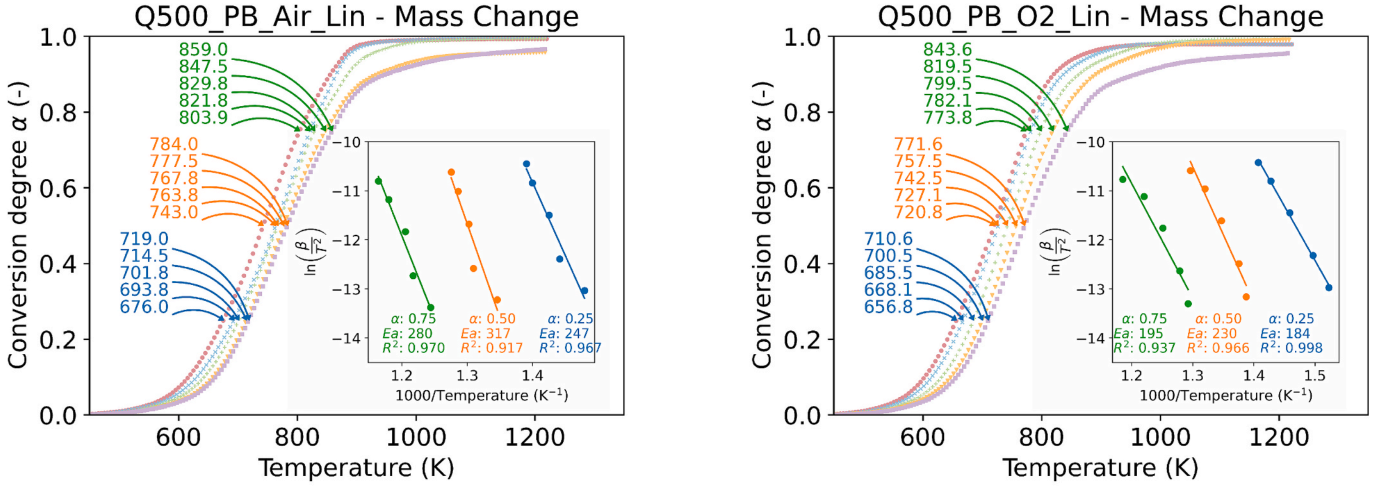

a.

b.

Fig. 11. Kissinger–Akahira–Sunose method applied to the TGA tests with linear heating rates with powder B.

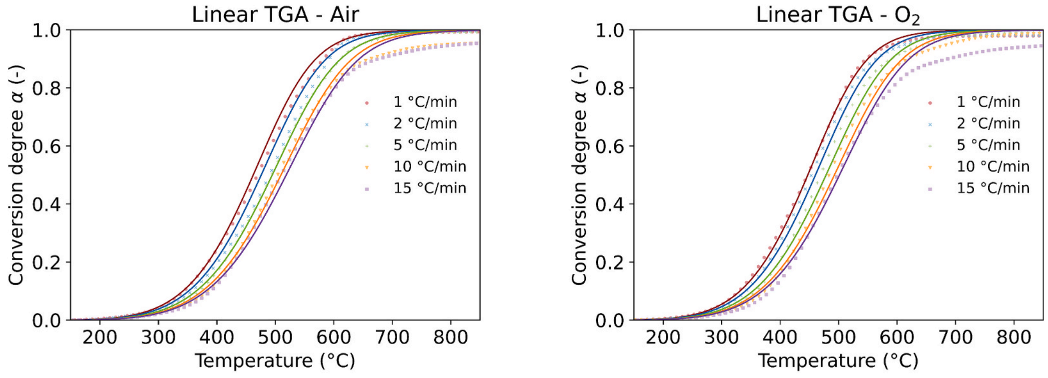

a.

b.

Fig. 12. Comparison between the truncated Sestak and Berggren model and experiments for the thermogravimetric analysis with heating linear rates from 1 to 15 °C on powder B.

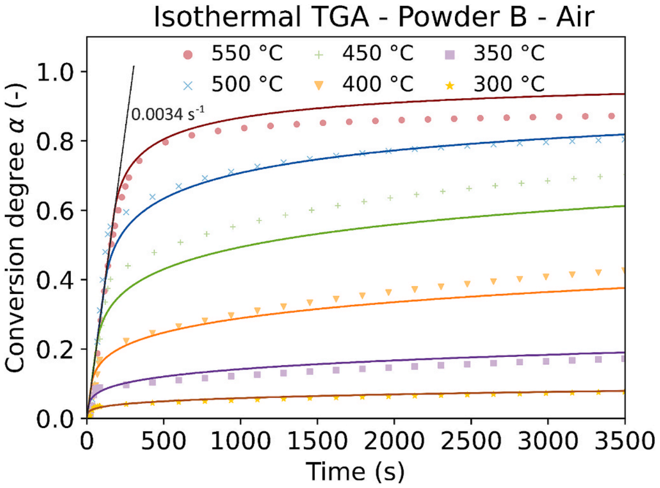

Fig. 13. Comparison between the truncated Sestak and Berggren model and experiments for the isothermal thermogravimetric analysis on powder B.

4.6. Discussion

4.6.1. Interpretation of the thermal analysis

The first conclusion that can be drawn from the TGA curves, both under isothermal condition as with a linear increase of the temperature, is that the rate of oxidation strongly increases with the temperature up to 570 °C, but also strongly decreases with the extent of oxidation. This is in agreement with a process limited by the diffusion of cations in the oxide layer. However, concerning the isothermal cases, it is quite obvious that under the present experimental configuration, the rate limiting process of the first stage is controlled by the external mass transfer of oxygen: the initial slopes are almost constant for various temperatures when the gas flow rate is kept constant and the slopes are directly correlated to the oxygen gas flow rate to sample mass ratio. In fact, we saw that the slopes increase with the gas flow rate, the concentration of oxygen, and decrease with increasing initial sample weight. Preventing external mass transfer limitations may be practically difficult. The usual operational change would be to increase the gas flow rate, but as a side effect, it may increase the temperature overshoot, thus compromising the isothermal conditions. One approach could be to dilute the iron in an inert solid to mitigate the collective heating effect. Larger particles with lower reactivity may also be less prone to external mass transfer limitations.

The second stage of isothermal oxidation experiments, on the other hand, seems to be limited by the oxide growth mechanism internal to the particles, as the gas flow rate and oxygen concentration have no notable influence. This second controlling factor is highly temperature dependent, thus the transition occurs at a higher extent of oxidation at higher temperatures. The transition from the first stage to the second can be explained as follow: because of the temperature overshoot, the gas-controlled stage – virtually insensitive to temperature – stays limiting to a larger extent than if there were no temperature overshoot, i.e. in perfect isothermal conditions. After the temperature overshoot, the particles cool down to the set temperature and the growth-controlling phenomenon becomes abruptly the limiting factor. This is particularly visible for the cases utilizing pure oxygen, as in Fig. 5: the temperature overshoot is particularly high, which results in discontinuous oxidation regimes. A gradual increase of the temperature, that is stepwise, as in Fig. 4, or with a constant heating rate, avoid partly or totally the gas-transport limitations.

Now, the deceleration of the oxidation rate with the extent of oxidation during this second stage should be discussed in depth. The primary reason could be the limitation by ionic diffusion at the particle scale due to the formation of an oxide of increasing thickness, analogous to the governing mechanism for flat surfaces. However, the decrease in the reactivity with the extent of oxidation is in the case of powders much stronger, and classical reaction models are not suited. The decrease in reactivity is most likely multifactorial. One possible explanation is interparticle sintering, which has a dual effect: it reduces the surface area and accelerates the ionic diffusion of iron towards the interparticle contact, increasing locally the thickness of the oxide layer. The synergy impact of sintering and oxidation processes will depend on the fundamental mechanisms governing both processes, which need to be investigated in detail in further work. However, we can assume that the sintered sample remains permeable to oxygen. Even if the SEM images showed a certain disparity in the morphology of the oxide layer formed at the surface and in the center of the sample, the degree of oxidation was quite homogeneous throughout the sample. In addition, variation of the initial sample weight did not affect the second stage of the oxidation in the isothermal cases. Spielmann et al. were able to prevent sintering by dilution with boron nitride, which clearly demonstrated that sintering only diminishes the rate of oxidation above 600 °C. Further explanations for the strong deceleration should then be hypothesized. There could be initially the presence of a negative space charge, as stipulated by the thin film theory, whose influence wanes after a certain oxide scale size. The theory of Boggs et al. [32] could also apply to the present case: at an early stage, magnetite could be formed directly by reaction with air, as it exceeds the speed of hematite nucleation. Once the hematite layer has nucleated, magnetite forms at the magnetite/hematite layer with a reduced rate. The SEM and XRD showed only a small presence of hematite in the sample oxidized at 400 °C for two hours. This theory could be verified in later studies by stopping the oxidation at an early stage or by performing in-situ XRD.

The study of thermal analysis with constant heating rates brings further understanding of the oxidation process. In this case, the process is continuous and we can rule out gas transport limitations, as the curves mostly overlap for experiments with varying sample weights. Thus, limitations due to internal growth mechanisms prevail under the present conditions. It is noticeable that the oxidation process starts at low temperatures, but extends over a very broad temperature range. The curves are very close to each other, indicating a high activation energy. An activation energy has been estimated, but with uncertainties because of how close the curves are. A small deviation in the experimental measurements has a large effect on the value found. The present estimated value (220 kJ/mol) is quite close to the activation energy of the self-diffusion coefficient of iron in magnetite (230 kJ/mol [31]), but it corresponds more likely to an apparent activation energy, including multiple physical phenomena as previously detailed. The SEM images at 455 °C were quite similar to the ones from the isothermal case at 400 °C. The XRD analysis also showed a prevalence of magnetite. An undisclosed point of the present study is how the sample proceeds to fully oxidize to hematite. In fact, cases with low heating rates (1 or 2 K/min) reached a complete oxidation at temperatures around 570 °C. SEM imaging of such a sample could shed light on this final stage. Tests at higher heating rates do not achieve complete oxidation, which can be explained as follows: the remaining iron forms wüstite above 570 °C and further oxidation of wüstite to magnetite or hematite is slower. Thus, the sample may have very little iron left, but the degree of oxidation is less than 1 due to the presence of wüstite. The XRD for the sample oxidized to 700 °C showed some residual iron, but a portion is attributable to the disproportionation reaction of wüstite during the cooling process. The authors recommend rapid quenching of the sample in future studies for oxidation above 570 °C.

4.6.2. Proposed growth mechanism of single particles

On the basis of the thermal analysis and its interpretation, we propose the mechanism illustrated in Fig. 14 for the oxidation of single iron particles under 570 °C, which bares many similarities to the one of Bertrand et al. [29] on pure iron sheets oxidized at low temperatures (260–400 °C). The oxidation is primarily controlled by the outward

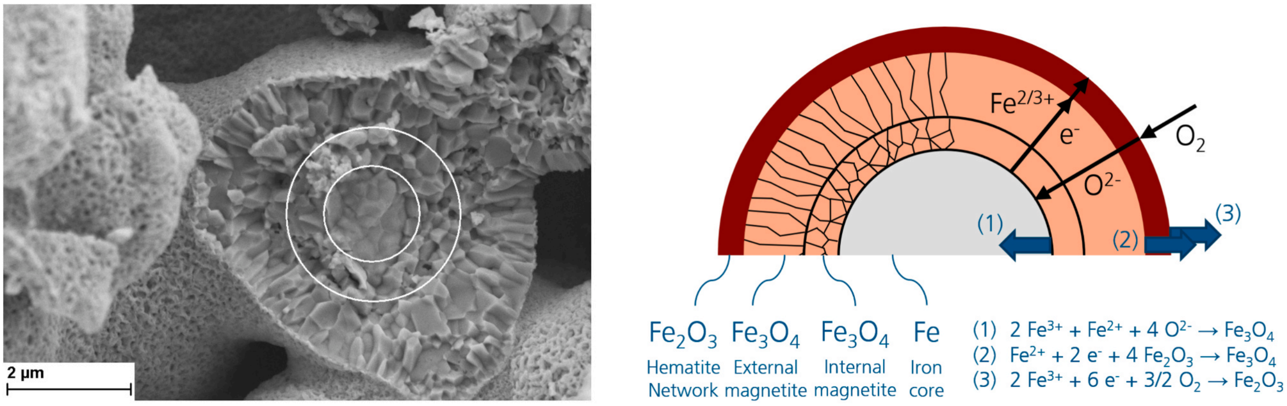

a.

b.

Fig. 14. a. cross-section of a particle oxidized up to 455 °C and b. mechanism illustrating the morphology of the iron oxides formed from the outward diffusion of Fe cations and the inward diffusion of oxygen anions.

growth of magnetite. Ferrous ions Fe^{2+}, ferric ions Fe^{3+}, and electrons migrate to the magnetite/hematite interface and hematite/air interface. Hematite grows according to the reaction:

$$2\ Fe^{3+} + 6\ e^- + 3/2\ O_2 \rightarrow Fe_2O_3 \tag{11}$$

But hematite is also consumed by the reaction responsible for the outward growth of magnetite:

$$Fe^{2+} + 2\ e^- + 4\ Fe_2O_3 \rightarrow Fe_3O_4 \tag{12}$$

If the process was only controlled by outward growths, porous cores should form. However, in the SEM image of the broken particle, no gap is visible, and in the cross-section images of individual particles, only isolated pores are evidenced. Thus, the oxidation process is completed by ionization of oxygen and inward short-circuit transport to the iron/magnetite interface:

$$2\ Fe^{3+} + Fe^{2+} + 4\ O^{2-} \rightarrow Fe_3O_4 \tag{13}$$

The SEM image of the fractured particle tends to validate this inward growth, as we can identify an outer layer having a columnar structure and an inner layer more equiaxed, similar to the duplex layer description of Atkinson et al. [12]. The cross-sections, on the other hand, show that small pores might form in the inner magnetite layer, when contact between the iron core and oxide is lost.

Following the proposed mechanism, all three growth rates are interdependent: the hematite growth depends on the total migration path, the magnetite outward growth depends on the availability of hematite, while the inward growth cannot proceed prior to the outward growth. This is evidenced by the uniformity of the layers around any particle and among multiple particles.

4.6.3. *Future research directions*

Research on the oxidation of iron particles is uncharted territory in comparison to, for example, the oxidation of iron strips or the reduction of iron oxides. In this regard, recommendations for future research directions can be drawn based on this present early study.

Strong sintering was experienced when temperatures around 700 °C were aimed. For kinetic studies, and in order to derive the intrinsic rates of oxidation, it appears essential to limit the sintering and its effects. These effects might be furthermore prejudicial to the cyclic oxidation/reduction, especially in a fixed setup where particles are closed to each other. Sintering is enhanced by mechanical pressure and temperature. When high temperatures are sought, dilution appears to be an effective solution [8,9]. Ceramic-stabilized iron particles, as developed for the iron steam process [59], could be a further option to explore to permit cyclic operations. The effect of sintering for dust firing, where particles are relatively isolated from each other remains to be determined, but fouling is one of the common issues reported in combustion chamber operations [60].

The proposed mechanism has been established from the apparent similarity between a mechanism proposed in the literature for iron strips and a couple of SEM images of partially oxidized particles. A thorough validation will necessitate the gathering of more images, or the use of alternative characterization techniques, eventually in-situ. In particular, analysis at various extents of oxidation would be of great assets, for example at the very early stage, or, on the opposite, close to completion of the oxidation. It could not be determined, in the context of this study, whether both magnetite and hematite form at the early stages, or if the nucleation of hematite only starts after the growth of the magnetite layer to a certain extent. Another question mark is how does the complete oxidation of magnetite to hematite proceed when low heating rates are used.

For iron dust firing, it is expected that each particle starts oxidizing to magnetite and hematite up to 570 °C and furthermore to wüstite, magnetite and hematite up to the ignition temperature. The state of the particle is decisive, for example, for the probability of ignition or flame propagation. Further work will thus be needed concerning the kinetic modeling. Standard gas-kinetic modeling relying on a unique conversion degree might be limited. From the current knowledge, particle size is a major characteristic influencing the rate of oxidation, thus models including a particle size distribution are expected to be more accurate. More detailed models could even be based on a particle oxidation mechanism as proposed in this study, where the evolution of the single oxide species is resolved, which would lead to accurate determination of the ignition process or of the heat release rates.

5. Conclusions

This comprehensive thermal analysis of the oxidation of iron powders, based on thermogravimetric experiments, microstructural characterization, kinetic modeling, and a focus up to 570 °C, sheds light on the underlying oxidation mechanism. A large body of literature is available on the oxidation of metals in general and specifically on the oxidation of iron sheets. A dedicated section has reviewed the existing literature in detail and the first conclusion that can be drawn at the end of this study is the great similarity in the case of powder. The TGA test campaign that has been conducted comprises non-isothermal oxidation tests at constant heating rates of 1, 2, 5, 10, and 15 °C/min and isothermal experiments with temperatures ranging from 300 to 700 °C.

Two powders were used as well as two thermogravimetric analyzers to ensure reproducibility of the results. Some parameters were varied, including oxidizing gas, gas flow rate, and initial solid weight. These experiments were completed with SEM and XRD analysis. The present study could show that under isothermal conditions, a first stage is controlled by external mass transport. It later switches to limitations from internal growth mechanisms; a step strongly temperature dependent, but also strongly hindered by the extent of oxidation. While this is in agreement with Wagner's theory, which predicts a decreasing growth rate with increasing oxide layer size, other phenomena could amplify this tendency, such as the inter-particle sintering shown by SEM images. The experiments with constant heating rates showed continuous profiles, and even a complete oxidation at low heating rates. To some extent, classical gas–solid kinetic methods can be used in the low temperature range of this study. Here an activation energy of about 220 kJ/mol was determined and the Sestak and Berggren model could reproduce isothermal and non-isothermal experiments. In general, the present findings suggest that the kinetic models and parameters derived on iron flat surfaces may not be suitable for iron powders. It should be noted, however, that the activation energy using the KAS method has a certain uncertainty, and that only the Sestak and Berggren model with high exponent values could give satisfactory agreement, and not more classical reaction models such as a shrinking core. At both 400 °C and 455 °C the main oxide is magnetite. At higher temperatures or heating rates, it may be necessary to account for the presence of both magnetite and wüstite, and multiple reaction mechanisms may be required. Finally, a detailed particle growth mechanism for a particle oxidized to about 50 % has been proposed, involving a duplex layer of magnetite surrounded by a thin layer of hematite.

CRediT authorship contribution statement

Quentin Fradet: Writing – review & editing, Writing – original draft, Visualization, Validation, Supervision, Software, Resources, Project administration, Methodology, Investigation, Formal analysis, Data curation, Conceptualization. **Syafinah Fong:** Validation, Resources, Investigation, Data curation. **Michalina Kurnatowska:** Validation, Resources, Investigation, Data curation. **Antonio Soria-Verdugo:** Writing – review & editing, Validation, Resources, Investigation, Data curation. **Laurine Choisez:** Writing – review & editing, Writing – original draft, Visualization, Validation, Resources, Methodology, Investigation, Data curation. **Uwe Riedel:** Writing – review & editing, Supervision, Project administration, Funding acquisition.

Declaration of competing interest

The authors declare that they have no known competing financial interests or personal relationships that could have appeared to influence the work reported in this paper.

Acknowledgements

This work was performed within the DLR project IronCircle® and the cluster project Clean Circles.

Appendix A. Supplementary material

Supplementary data to this article can be found online at https://doi.org/10.1016/j.fuel.2025.135866.

Data availability

Data will be made available on request.

References

[1] Bergthorson JM. Recyclable metal fuels for clean and compact zero-carbon power. Prog Energy Combust Sci 2018;68:169–96.

[2] Bergthorson JM, Goroshin S, Soo MJ, Julien P, Palecka J, Frost DL, et al. Direct combustion of recyclable metal fuels for zero-carbon heat and power. Appl Energy 2015;160:368–82.

[3] Clean circles; 2021. [Online]. Available: www.clean-circles.de. [Accessed 29 9 2021].

[4] Iron fuel technology.

[5] Mi X, Fujinawa A, Bergthorson JM. A quantitative analysis of the ignition characteristics of fine iron particles. Combust Flame 2022;240:112011.

[6] Mich J, Braig D, Gustmann T, Hasse C, Scholtissek A. A comparison of mechanistic models for the combustion of iron microparticles and their application to polydisperse iron-air suspensions. Combust Flame 2023;256:112949.

[7] Ning D, Li Y, Li T, Böhm B, Dreizler A. Size-resolved ignition temperatures of isolated iron microparticles. Combust Flame 2024;270:113779.

[8] Spielmann J, Braig D, Streck A, Gustmann T, Kuhn C, Reinauer F, et al. Exploring the oxidation behavior of undiluted and diluted iron particles for energy storage: Mössbauer spectroscopic analysis and kinetic modeling. PCCP 2024;26(17):13049–60.

[9] Kuhn C, Knapp A, Deutschmann MP, Spielmann J, Tischer S, Kramm UI, et al. Iron as recyclable metal fuel: unraveling oxidation behavior and cyclization effects through thermogravimetric analysis, wide-angle X-ray scattering and Mössbauer spectroscopy. ChemSusChem 2024;17(15):e202400351.

[10] Bruce IA. The oxidation behaviour of sintered iron. University of Aston; 1991.

[11] Lawless KR. The oxidation of metals. Rep Prog Phys 1974;37(2):231–316.

[12] Atkinson A. Transport processes during the growth of oxide films at elevated temperature. Rev Mod Phys 1985;57(2):437–70.

[13] Mott NF. The theory of crystal rectifiers. Proc R Soc Lond A 1939;171(944):27–38.

[14] Cabrera N, Mott NF. Theory of the oxidation of metals. Rep Prog Phys 1949;12(1):163–84.

[15] Wagner C. Beitrag zur theorie des anlaufvorgangs. Zeitschrift für Physikalische Chemie 1933;21B(1):25–41.

[16] Wagner C. Beitrag zur theorie des anlaufvorganges. II. Zeitschrift für Physikalische Chemie 1936;32B(1):447–62.

[17] Atkinson A. Wagner theory and short circuit diffusion. Mater Sci Technol 1988;4(12):1046–51.

[18] Davies MH, Simnad MT, Birchenall CE. On the mechanism and kinetics of the scaling of iron. JOM 1951;3(10):889–96.

[19] Païdassi J. Sur la cinetique de l'oxydation du fer dans l'air dans l'intervalle 700–1250°C. Acta Metall 1958;6(3):184–94.

[20] Atkinson A, Smart DW. Transport of nickel and oxygen during the oxidation of nickel and dilute nickel/chromium alloy. J Electrochem Soc 1988;135(11):2886–93.

[21] Caplan D, Hussey RJ, Sproule GI, Graham MJ. The effect of FeO grain size and cavities on the oxidation of Fe. Corros Sci 1981;21(9–10):689–711.

[22] Garnaud G, Rapp RA. Thickness of the oxide layers formed during the oxidation of iron. Oxid Met 1977;11(4):193–8.

[23] Simmons GW, Kellerman E, Leidheiser H. The oxidation of iron as studied by conversion electron Mössbauer spectroscopy. Corrosion 1973;29(6):227.

[24] Caplan D, Cohen M. Scaling of iron at 500°C. Corros Sci 1963;3(3). 139-IN2.

[25] Hussey RJ, Sproule GI, Caplan D, Graham MJ. The growth and structure of oxide films formed on Fe in O2 and CO2 at 550C. Oxid Met 1977;11(2):65–79.

[26] Caplan D, Cohen M. Effect of cold work on the oxidation of iron from 400–650 °C. Corros Sci 1966;6(7):321–35.

[27] Caplan D, Sproule GI, Hussey RJ. Comparison of the kinetics of high-temperature oxidation of Fe as influenced by metal purity and cold work. Corros Sci 1970;10(1):9–17.

[28] Hussey RJ, Graham MJ. Some observations on void formation in Fe3O4 layers on Fe. Corros Sci 1981;21(3):255–8.

[29] Bertrand N, Desgranges C, Poquillon D, Lafont MC, Monceau D. Iron oxidation at low temperature (260–500 °C) in air and the effect of water vapor. Oxid Met 2010;73(1–2):139–62.

[30] Pujilaksono B, Jonsson T, Halvarsson M, Svensson J-E, Johansson L-G. Oxidation of iron at 400–600°C in dry and wet O2. Corros Sci 2010;52(5):1560–9.

[31] Himmel L, Mehl RF, Birchenall CE. Self-diffusion of iron in iron oxides and the Wagner theory of oxidation. JOM 1953;5(6):827–43.

[32] Boggs WE, Kachik RH, Pellissier GE. The effect of oxygen pressure on the oxidation of zone-refined iron. J Electrochem Soc 1965;112(6):539.

[33] Szklarska-Smialowska Z, Jurek J. Ellipsometric studies on iron oxide film growth at 100 to 350 C. Corrosion 1976;32(7):294–7.

[34] Sakai H, Tsuji T, Naito K. Oxidation of iron in air between 523 and 673 K. J Nucl Sci Technol 1985;22(2):158–61.

[35] Graham MJ, Ali SI, Cohen M. Low temperature oxidation (24° to 200°C) and krypton adsorption studies on polycrystalline and single crystal iron surfaces. J Electrochem Soc 1970;117(4):513.

[36] Channing DA, Graham MJ. A study of iron oxidation processes by Mössbauer spectroscopy. Corros Sci 1972;12(3):271–89.

[37] Reddy K, Cooper AR. Oxygen diffusion in MgO and α-Fe2O3. J Am Ceram Soc 1983;66(9):664–6.

[38] Takagi R. Growth of oxide whiskers on metals at high temperature. J Phys Soc Jpn 1957;12(11):1212–8.

[39] Svedung I, Hammar B, Vannerberg N-G. The effect of recrystallization on the oxide scale composition and growth of whiskers during the oxidation of pure iron. Oxid Met 1973;6(1):21–44.

[40] Voss DA, Butler EP, Mitchell TE. The growth of hematite blades during the high temperature oxidation of iron. Metall Trans A 1982;13(5):929–35.

[41] Yuan L, Wang Y, Cai R, Jiang Q, Wang J, Li B, et al. The origin of hematite nanowire growth during the thermal oxidation of iron. Mater Sci Eng B 2012;177 (3):327–36.

[42] Lupan O, Postica V, Wolff N, Polonskyi O, Duppel V, Kaidas V, et al. Localized synthesis of iron oxide nanowires and fabrication of high performance nanosensors based on a single Fe2O3 nanowire. Small 2017;13(16):1602868.

[43] Lysenko EN, Surzhikov AP, Zhuravkov SP, Vlasov VA, Pustovalov AV, Yavorovsky NA. The oxidation kinetics study of ultrafine iron powders by thermogravimetric analysis. J Therm Anal Calorim 2014;115(2):1447–52.

[44] Wen D, Song P, Zhang K, Qian J. Thermal oxidation of iron nanoparticles and its implication for chemical-looping combustion. J Chem Technol Biotechnol 2011;86 (3):375–80.

[45] Mandilas C, Karagiannakis G, Konstandopoulos AG, Beatrice C, Lazzaro M, Di Blasio G, et al. Study of oxidation and combustion characteristics of iron nanoparticles under idealized and enginelike conditions. Energy Fuel 2016;30(5): 4318–30.

[46] Zhang CM, Jin J, He DD, Zhang H, Jiang J, Gao XY, et al. Reaction mechanism study on combustion of micro nanometer iron powder. Adv Mat Res 2012; 535–537:459–64.

[47] Korshunov AV. Kinetics of the oxidation of an electroexplosion iron nanopowder during heating in air. Russ J Phys Chem B 2012;6(3):368–75.

[48] Lysenko EN, Surzhikov AP, Nikolaev EV, Vlasov VA, Zhuravkov SP. The oxidation kinetic study of mechanically milled ultrafine iron powders by thermogravimetric analysis. J Therm Anal Calorim 2018;134(1):307–12.

[49] Fedoryk M, Stelzner B, Harth S, Trimis D. Laminar burning velocity measurements and stability map determination of Fe-N2/O2 mixtures in a tube burner; 2023.

[50] Sarkar C, Hirani H. Effect of particle size on shear stress of magnetorheological fluids. Smart Sci. 2015;3(2).

[51] Soria-Verdugo A, Morgano MT, Mätzing H, Goos E, Leibold H, Merz D, et al. Comparison of wood pyrolysis kinetic data derived from thermogravimetric experiments by model-fitting and model-free methods. Energ Conver Manage 2020;212:112818.

[52] Fradet Q, Kurnatowska M, Riedel U. Thermochemical reduction of iron oxide powders with hydrogen: review of selected thermal analysis studies. Thermochim Acta 2023;726:179552.

[53] Kissinger HE. Reaction kinetics in differential thermal analysis. Anal Chem 1957; 29(11):1702–6.

[54] Kissinger HE. Variation of peak temperature with heating rate in differential thermal analysis. J Res Nat Bur Stand 1956;57(4):217.

[55] Akahira T, Sunose T. Method of determining activation deterioration constant of electrical insulating materials. Res Rep Chiba. Inst Technol (Sci Technol) 1971;16.

[56] Vyazovkin S, Burnham AK, Criado JM, Pérez-Maqueda LA, Popescu C, Sbirrazzuoli N. ICTAC kinetics committee recommendations for performing kinetic computations on thermal analysis data. Thermochim Acta 2011;520(1–2):1–19.

[57] Choisez L, Hemke K, Özgün Ö, Pistidda C, Jeppesen H, Raabe D, et al. Hydrogen-based direct reduction of combusted iron powder: deep pre-oxidation, reduction kinetics and microstructural analysis. Acta Mater 2024;268:119752.

[58] Gleeson B, Hadavi S, Young DJ. Isothermal transformation behavior of thermally-grown wüstite. Mater High Temp 2000;17(2):311–8.

[59] Göthel J, Burkmann KJ, Volkova O. Review and evaluation of ceramic-stabilized iron oxides for use as energy storage based on iron-steam process. Steel Res Int 2025;96(5):2400265.

[60] van Rooij NE. Development of iron powder boilers for industry. Eindhoven: Eindhoven University of Technology; 2025.